Modeling of Planar Multilayered Periodic Arrays Using the Method of Lines

Éric Choinière, *Student Member ACES* and Jean-Jacques Laurin

***Abstract*— This paper presents an implementation of the Method of Lines, a semi-analytical method, for the numerical modeling of radiating stratified periodic structures composed of dielectric layers interspersed with metallic patches and slots. Beam scanning antenna arrays and frequency selective surfaces (FSS) are among possible applications. The combined use of the *Modified Biconjugate Gradient Squared method with Stabilization*, an iterative resolution method, together with the Fast Fourier Transform allows for the analysis of a wide array of problems using uniform, high discretization density by considerably speeding up the resolution process and drastically reducing memory requirements. Periodic FSS and slot coupled patch array antennas were simulated. A comparison of simulation results with available literature allows validation of the new approach.**

***Index Terms*— Method of Lines, Antenna Arrays, Frequency Selective Surfaces, Multilayered structures, Conjugate Gradient FFT technique.**

I. INTRODUCTION

Large multilayered printed array antennas with beam scanning capabilities [1] and frequency selective surfaces (FSS) are structures of increasing interest for satellite-based telecommunications. Both applications, presented in Figure 1, can essentially be formulated as *planar multilayered periodic arrays* of metallic patches and/or slots. The use of periodic conditions to model the behavior of these arrays is justified by their large size (typically, 100×100 elements).

The coupling of surface waves in these structures is of great importance for incidence angles away from broadside. Such coupling can lead to scan blindness at specific angles, with important effects on the impedance over a broad angular scan range. In addition, the trend toward multi-frequency antennas in space applications contributes to the increase in complexity of printed antenna structures, for instance through the combination of several dielectric substrates, metallic elements and coupling slots. These two factors emphasize the need for accurate analysis tools oriented toward such structures.

Previous work has been done on full-wave modeling techniques for these types of structures [2], [3], [4], [5], mostly using the method of moments and its derivatives. In this communication, we present a novel and modular modeling technique based on the Method of Lines [6] (MoL), a full-wave semi-analytical technique based on the partial discretization of the solution space. Previous papers ([7],[8], [9]) have used the MoL to model metallic grating structures for FSS applications which required discretization of a single variable (1D discretization). Here we present a model allowing for multilayered, planar arbitrary metallic patterns (2D discretization). In addition to allowing plane wave excitation for FSS applications, it supports the microstrip line slot coupling scheme which is widely used in printed antenna arrays.

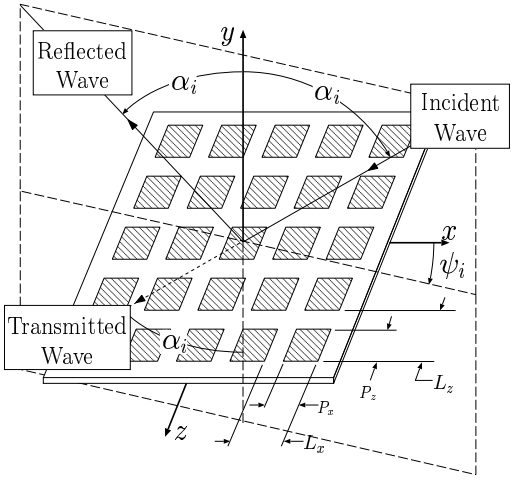

(a) Frequency selective surface.

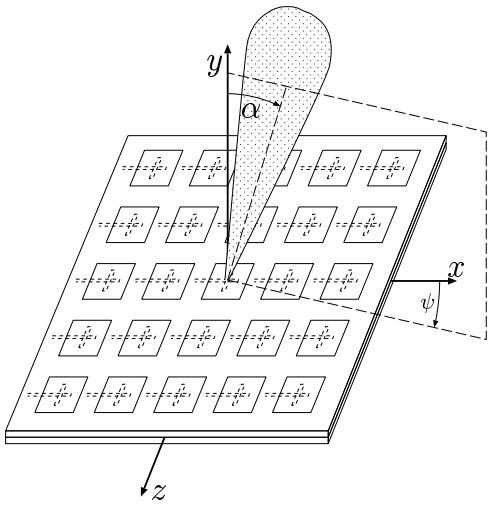

(b) Phased array antenna.

Fig. 1. Two types of planar periodic array structures.

This work was supported by the Natural Sciences and Engineering Research Council of Canada and by the Communications Research Centre of Canada.

Éric Choinière is with the Radiation Laboratory, Electrical Engineering and Computer Science Department, University of Michigan, 1301 Beal Avenue, Ann Arbor, MI 48109-2122, USA, echoinie@umich.edu

Jean-Jacques Laurin is with the Department of Electrical Engineering, École Polytechnique de Montréal, P.O. Box 6079, Downtown Station, Montreal, Quebec, H3C 3A7, Canada, laurinj@grmes.polymtl.ca

The semi-analytical nature of the MoL makes it particularly well-suited for the analysis of planar multilayered structures. Some of its merits are:

- it is based on surface (as opposed to volume) discretization of the interfaces of each layer;
- it does not require the use of analytic Green's functions;
- it does not involve numerical integrals, which circumvents any integration of poles;
- it does not rely on the choice of basis functions.

A preliminary study of this technique with linear arrays was presented earlier [10]. The generalization of the technique for planar, multilayered structures poses challenges with respect to memory requirements and computing time. In fact, the main drawbacks of the MoL with uniform discretization are its high memory and computing time requirements associated with high levels of discretization. One of the important features of the technique presented here is that it uses the properties of periodic boundary conditions to allow great savings in memory and computing time, through the use of the fast Fourier transform and an iterative resolution method, the modified biconjugate gradient squared method with stabilization (Bi-CGSTAB2) [11]. This technique gives access to the merits of the MoL at reasonable memory and computing costs.

The main objective of this work is to establish the functionality of our MoL-based model for the above-mentioned structures. Extensions to the existing MoL techniques for the problems at hand will be briefly presented, and validations with typical cases of interest will be carried out. Many of the mathematical details, presented elsewhere [12], have been omitted from the paper for conciseness.

II. General formulation

A. Definition of the unit cell of the periodic structure

As illustrated in Figure 2, the analysis of a periodic structure is simplified by considering one single cell and applying the appropriate periodic boundary conditions on its sides. The fields and currents are not properly periodic, since we want to allow for a linear phase progression corresponding to the angles ψ_i, α_i of an incident wave on an FSS or the angles ψ, α of the main antenna beam for a phased array (see Figure 1). These angles determine the fundamental spatial frequencies $k_{x0} = -k_0 \sin\alpha^i \cos\psi^i = k_0 \sin\alpha\cos\psi$ and $k_{z0} = -k_0 \sin\alpha^i \sin\psi^i = k_0 \sin\alpha \sin\psi$ for all fields in the solution, where $k_0 = \frac{2\pi}{\lambda_0}$ is the wavenumber in vacuum. By applying the phase normalization factor $e^{j(k_{x0}x + k_{z0}z)}$ to all electromagnetic quantities, we get periodic distributions for all normalized quantities.

Figure 3 presents the general topology for a single cell inside a planar multilayered periodic structure. It is composed of a number of homogeneous dielectric layers interspersed with arbitrary metallic patterns (e.g. patches, slots). By adding a periodic source and absorbing boundary conditions (ABC) over the top layer and under the bottom layer, our generic problem is completely specified. We will be looking for a solution that:

1) Satisfies the simple wave equation for source-free media in all dielectric layers;

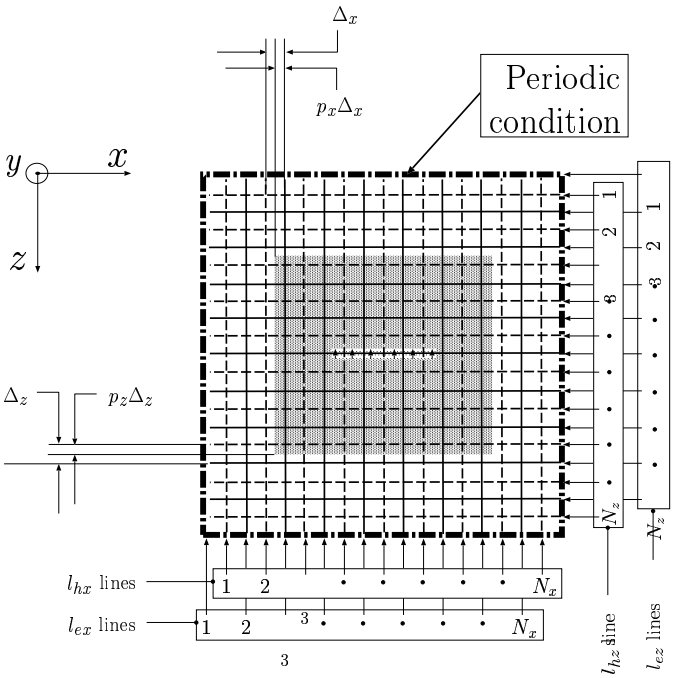

Fig. 2. Discretization scheme of one cell with boundary conditions.

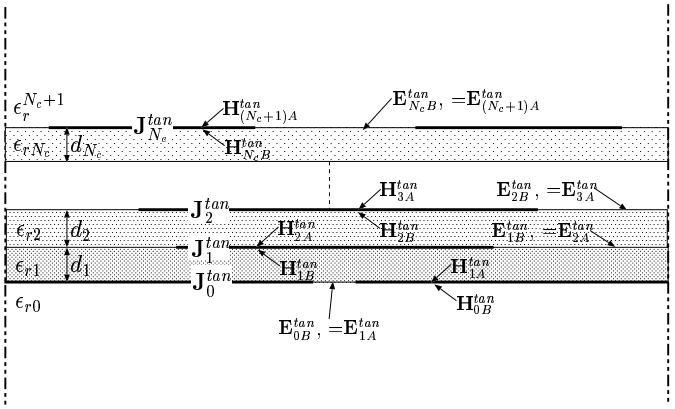

Fig. 3. General topology of a multilayered periodic cell with employed notation.

2) Satisfies the boundary conditions at all interfaces between dielectric layers, including the tangential magnetic field discontinuity due to surface currents on the metallic patterns;
3) Satisfies the periodic boundary conditions for all normalized fields;
4) Satisfies the absorbing boundary conditions (ABC) at the interface between the top layer and vacuum, as well as at the interface between the bottom layer and vacuum.

B. Discretization of Helmholtz's equation

In every distinct dielectric layer, as well as in the free space regions over and under the structure (see Figure 3), the z-component of the electric and magnetic fields satisfy the Helmholtz equation [6]. In the MoL formulation, the partial derivatives with respect to x and z are approximated by finite

differences and the analytical derivative with respect to y is preserved in the Laplacian operator. Doing so, the Helmholtz equation is written for both $\mathbf{E}_z^\ell$ and $\mathbf{H}_z^\ell$:

$$\left(\frac{d}{d^2y} - \frac{\hat{\mathbf{P}}_x^e}{\Delta_x^2} - \frac{\hat{\mathbf{P}}_z^e}{\Delta_z^2} + \epsilon_r k_0^2 \hat{\mathbf{I}}\right) \mathbf{E}_z^\ell = 0 \tag{1}$$

$$\left(\frac{d}{d^2y} - \frac{\hat{\mathbf{P}}_x^h}{\Delta_x^2} - \frac{\hat{\mathbf{P}}_z^h}{\Delta_z^2} + \epsilon_r k_0^2 \hat{\mathbf{I}}\right) \mathbf{H}_z^\ell = 0 \tag{2}$$

where ϵ_r is the relative permittivity of any particular layer, while $\mathbf{E}_z^\ell$ and $\mathbf{H}_z^\ell$ are vectors containing the electric and magnetic fields, discretized in the x-z plane.

The positions of the N_x and N_z samples along the x and z directions, respectively, are indicated on Figure 2. $\hat{\mathbf{P}}_x^h$, $\hat{\mathbf{P}}_z^h$, $\hat{\mathbf{P}}_x^e$ and $\hat{\mathbf{P}}_z^e$ are matrix operators that implement the double partial derivatives using finite differences along lines l_{h_x}, l_{h_z}, l_{e_x} and l_{e_z}, respectively, as shown on Figure 2. Periodic boundary conditions along the x and z directions are built into these four operators. More specifically, these matrix operators are obtained from $\mathbf{P}_{x,z}^e = \mathbf{D}_{x,z}^* \mathbf{D}_{x,z}$ and $\mathbf{P}_{x,z}^h = \mathbf{D}_{x,z} \mathbf{D}_{x,z}^*$, where $\mathbf{D}_{x,z}$ are the 1-D difference operators in which the periodic conditions are embedded [6].

C. Diagonalization of Helmholtz's equation

Matrix equations (1) and (2) are sets of $N_x \times N_z$ single-variable coupled differential equations. Following a diagonalization procedure developed in [6], these equations can be rewritten in the form:

$$\left(\frac{d}{d^2y} - {\mathbf{k}_y}^2\right) \overline{\mathbf{E}}_z^\ell = 0 \tag{3}$$

$$\left(\frac{d}{d^2y} - {\mathbf{k}_y}^2\right) \overline{\mathbf{H}}_z^\ell = 0 \tag{4}$$

where ${\mathbf{k}_y}^2$ is a diagonal matrix given by:

$${\mathbf{k}_y}^2 = \left(\frac{\hat{\boldsymbol{\lambda}}_x}{\Delta_x}\right)^2 + \left(\frac{\hat{\boldsymbol{\lambda}}_z}{\Delta_z}\right)^2 - \epsilon_r k_0^2 \hat{\mathbf{I}} \tag{5}$$

$\overline{\mathbf{E}}_z^\ell$ and $\overline{\mathbf{H}}_z^\ell$ correspond to $\mathbf{E}_z^\ell$ and $\mathbf{H}_z^\ell$ expressed in the eigenvector (transformed) domain. $\hat{\boldsymbol{\lambda}}_x$ and $\hat{\boldsymbol{\lambda}}_z$ are eigenvalue diagonal matrices depending on N_x, N_z and the source wavenumbers k_{x0} and k_{z0}.

D. Construction of a general system of equations

Defining a general algorithm to build a system of equations from any problem involving a bi-dimensionally periodic multilayered structure is key to the versatility of our formulation. The objective here is to formulate the electromagnetic problem of our multilayered structure as a linear system of equations with the unknowns being, alternatively, the tangential electric field samples on the un-metalized parts of each interface or the surface current density samples on the metalized parts of the interfaces. The unknowns can also be chosen as the tangential E-field samples on some interfaces and the surface current density samples on the other ones. To preserve the generality of the formulation, a homogeneous system of equations will first be derived. The source problem will then be addressed by setting some of the unknowns to defined values and solving for the remaining unknowns.

Equations (3) and (4) can be solved analytically for the z-directed fields in the transformed domain. A homogeneous system of equations is formed by enforcing the boundary conditions at each interface on the space-domain fields obtained from a superposition of the transformed-domain analytic solutions.

1) Intermediate layer hybrid parameters: Within any dielectric layer, the analytic solutions to (3) and (4) for all modes in the transformed domain are given by:

$$\overline{E}_{zi}^\ell = A_i \cosh(k_{yi} y) + B_i \sinh(k_{yi} y) \tag{6}$$

$$\overline{H}_{zi}^\ell = C_i \cosh(k_{yi} y) + D_i \sinh(k_{yi} y) \tag{7}$$

where the real and imaginary parts of k_{yi} are positive, i.e. $\Re(k_{yi}) > 0$ and $\Im(k_{yi}) > 0$ with $i = 1, 2, ..., N_x N_z$. The k_{yi}'s are obtained from the positive root of (5). This assumption, together with source-free Maxwell's equations, results in hybrid parameters relating the transformed tangential electric and magnetic field samples on both sides of any dielectric layer. These can be written as:

$$\begin{bmatrix} \overline{\mathbf{E}}_m^{tan} \\ \overline{\mathbf{H}}_m^{tan} \end{bmatrix}_{y=y_{top}} = \begin{bmatrix} \overline{\mathbf{V}}_m & \overline{\mathbf{Z}}_m \\ \overline{\mathbf{Y}}_m & \overline{\mathbf{V}}_m \end{bmatrix} \begin{bmatrix} \overline{\mathbf{E}}_m^{tan} \\ \overline{\mathbf{H}}_m^{tan} \end{bmatrix}_{y=y_{bot}} \tag{8}$$

where the tangential components along x and z on the top and bottom interfaces have been grouped following the same notation as in [6]:

$$\overline{\mathbf{E}}_m^{tan} = \begin{bmatrix} \overline{\mathbf{E}}_{x\,m}^\ell \\ -j\overline{\mathbf{E}}_{z\,m}^\ell \end{bmatrix} \qquad \overline{\mathbf{H}}_m^{tan} = \eta_0 \begin{bmatrix} -j\overline{\mathbf{H}}_{z\,m}^\ell \\ \overline{\mathbf{H}}_{x\,m}^\ell \end{bmatrix} \tag{9}$$

General forms for the sub-matrices $\overline{\mathbf{V}}_m$, $\overline{\mathbf{Y}}_m$ and $\overline{\mathbf{Z}}_m$ in (8) are given in [6]. These submatrices were modified for the specific bi-periodic case considered [12].

2) Absorbing boundary conditions: In the top and bottom free-space regions, the analytic solutions to (3) and (4) for all modes in the transformed domain are assumed to be traveling waves. This assumption constitutes a statement of the absorbing boundary conditions. The assumed modes in the top and bottom free-space regions are as follows:

$$\overline{E}_{zi}^\ell = A_i e^{\pm k_{yi} y} \qquad \overline{H}_{zi}^\ell = B_i e^{\pm k_{yi} y} \tag{10}$$

where the real and imaginary parts of k_{yi} are positive, i.e. $\Re(k_{yi}) > 0$ and $\Im(k_{yi}) > 0$ with $i = 1, 2, ..., N_x N_z$. The plus (+) and minus (-) signs refer, respectively, to the solutions in the bottom and top free-space regions. The k_{yi}'s are obtained from the positive root of equation (5). This assumed form, together with the source-free Maxwell's equations, allows to write absorbing boundary conditions in matrix form for the transformed fields. The ABC's on the top and bottom surfaces are implemented by establishing a relationship between

the tangential fields at the top and bottom of the solution domain [13]:

$$\overline{\mathbf{H}}^{tan} = \overline{\mathbf{W}}_T \overline{\mathbf{E}}^{tan}, \qquad y = y_{top} \tag{11}$$

$$\overline{\mathbf{H}}^{tan} = \overline{\mathbf{W}}_B \overline{\mathbf{E}}^{tan}, \qquad y = y_{bot} \tag{12}$$

where the subscripts T and B correspond, respectively, to the plus and minus signs and the compact vectors $\overline{\mathbf{E}}^{tan}$ and $\overline{\mathbf{H}}^{tan}$ are as defined in (9). The ABC's apply individually for every mode in the transformed domain. The formulations for $\overline{\mathbf{W}}_T$ and $\overline{\mathbf{W}}_B$ are given by [12]:

$$\overline{\mathbf{W}}_{T,B} = \pm k_0 \begin{bmatrix} \mathbf{k}_y^{-1}(\hat{\overline{\boldsymbol{\lambda}}}_z^2 - \epsilon_r \hat{\mathbf{I}}) & -j\mathbf{k}_y^{-1}\left(\overline{\boldsymbol{\lambda}}_z \otimes \overline{\boldsymbol{\lambda}}_x\right) \\ j\mathbf{k}_y^{-1}\left(\overline{\boldsymbol{\lambda}}_z \otimes \overline{\boldsymbol{\lambda}}_x\right) & \mathbf{k}_y^{-1}(\hat{\overline{\boldsymbol{\lambda}}}_x^2 - \epsilon_r \hat{\mathbf{I}}) \end{bmatrix} \tag{13}$$

3) Interface Boundary Conditions (IBC) in the transformed domain: The boundary conditions at each of the interfaces depend on the metallic layout at each interface as well as on the dielectric constants. Because of this, the IBC's are responsible for interactions among the spectral components obtained from the previous analytic treatment. In the transformed domain, the IBC's are:

$$\begin{aligned} \overline{\mathbf{E}}_m^{tan}\Big|_{y=y_{bot}} &= \overline{\mathbf{E}}_{(m-1)}^{tan}\Big|_{y=y_{top}} \\ \overline{\mathbf{H}}_m^{tan}\Big|_{y=y_{bot}} &= \overline{\mathbf{H}}_{(m-1)}^{tan}\Big|_{y=y_{top}} - \overline{\mathbf{J}}_{(m-1)}^{tan} \end{aligned} \qquad m = 1, 2, ..., N_c + 1 \tag{14}$$

where N_c is the number of dielectric layers comprised between the top and bottom free-space regions, and $\overline{\mathbf{J}}_{(m-1)}^{tan}$ represents the tangential surface current samples, in the transformed domain, on the interface between the $(m-1)^{\text{th}}$ and the m^{th} dielectric layers. More specifically, it is defined as:

$$\overline{\mathbf{J}}_m^{tan} = \eta_0 \begin{bmatrix} j\overline{\mathbf{J}}_{xm}^{\ell} \\ \overline{\mathbf{J}}_{zm}^{\ell} \end{bmatrix} \tag{15}$$

In the following, the IBC's will be used together with the hybrid parameters and ABC's to form the individual lines of our homogeneous system of equations.

4) Intermediate lines of the system of equations (lines $m = 1$ through $m = N_c - 1$): Using the intermediate layer hybrid parameters (8) for all dielectric layers, the IBC's (14) can be written in terms of the electric field only:

$$\overline{\mathbf{R}}_m \overline{\mathbf{E}}_{(m-1)B}^{tan} + \overline{\mathbf{Q}}_m \overline{\mathbf{E}}_{mB}^{tan} + \overline{\mathbf{R}}_{(m+1)} \overline{\mathbf{E}}_{(m+1)B}^{tan} + \overline{\mathbf{J}}_m^{tan} = 0 \qquad m = 1, 2, ..., N_c - 1 \tag{16}$$

5) First ($m = 0$) and last ($m = N_c$) lines of the system of equations: The analytic absorbing boundary conditions defined in II-D.2, together with the interface boundary conditions defined in II-D.3 can be used to derive, in a similar manner, the following two matrix equations:

$$\left(\overline{\mathbf{W}}_B + \overline{\mathbf{U}}_1\right) \overline{\mathbf{E}}_{0B}^{tan} + \overline{\mathbf{R}}_1 \overline{\mathbf{E}}_{1B}^{tan} + \overline{\mathbf{J}}_0^{tan} = 0 \tag{17}$$

$$\overline{\mathbf{R}}_{N_c} \overline{\mathbf{E}}_{(N_c-1)B}^{tan} + \left(\overline{\mathbf{U}}_{N_c} + \overline{\mathbf{W}}_T\right) \overline{\mathbf{E}}_{N_c}^{tan} + \overline{\mathbf{J}}_{N_c}^{tan} = 0 \tag{18}$$

where the $\overline{\mathbf{R}}_m$ and $\overline{\mathbf{U}}_m$ are defined in [12].

6) Homogeneous system of equations: Taking into account the couplings at all $N_c + 1$ interfaces and transforming back to the spatial domain leads to the following general system of equations:

$$\tilde{\mathbf{M}}_E \underbrace{\begin{bmatrix} \mathbf{E}_{0B}^{tan} \\ \mathbf{E}_{1B}^{tan} \\ \vdots \\ \mathbf{E}_{N_cB}^{tan} \end{bmatrix}}_{\tilde{\mathbf{E}}^{tan}} + \underbrace{\begin{bmatrix} \mathbf{J}_0^{tan} \\ \mathbf{J}_1^{tan} \\ \vdots \\ \mathbf{J}_{N_c}^{tan} \end{bmatrix}}_{\tilde{\mathbf{J}}^{tan}} = 0 \tag{19}$$

where $\tilde{\mathbf{M}}_E$ has the form:

$$\tilde{\mathbf{M}}_E = \begin{bmatrix} \mathbf{Q}_0 & \mathbf{R}_1 & & & & \\ \mathbf{R}_1 & \mathbf{Q}_1 & \mathbf{R}_2 & & & \\ & \mathbf{R}_2 & \mathbf{Q}_2 & \mathbf{R}_3 & & \\ & & \ddots & \ddots & \ddots & \\ & & & \mathbf{R}_{N_c-1} & \mathbf{Q}_{N_c-1} & \mathbf{R}_{N_c} \\ & & & & \mathbf{R}_{N_c} & \mathbf{Q}_{N_c} \end{bmatrix} \tag{20}$$

If we exclude imposed $\mathbf{E}$ and $\mathbf{J}$ sources, the system of equations (19) has twice as many unknowns as its number of equations. As described in [6], the system can be reduced to a homogeneous square system. At each interface we select $\mathbf{E}_{mb}^{tan}$ or $\mathbf{J}_m^{tan}$ to be the unknown quantity of interest. It is then possible to re-arrange equation (19) in the form:

$$\tilde{\mathbf{M}}_H \tilde{\mathbf{X}} + \tilde{\mathbf{Y}} = 0 \tag{21}$$

where $\tilde{\mathbf{X}}$ and $\tilde{\mathbf{Y}}$ contain, respectively, the selected and non-selected unknowns. The selection is done at each interface. Examples of $\tilde{\mathbf{X}}$ and $\tilde{\mathbf{Y}}$ are:

$$\tilde{\mathbf{X}} = \begin{bmatrix} \mathbf{J}_0^{tan} & \mathbf{E}_{1B}^{tan} & \mathbf{J}_2^{tan} \end{bmatrix}^T \tag{22}$$

$$\tilde{\mathbf{Y}} = \begin{bmatrix} \mathbf{E}_{0B}^{tan} & \mathbf{J}_1^{tan} & \mathbf{E}_{2B}^{tan} \end{bmatrix}^T \tag{23}$$

in a 3-interface model. The selection of variables forming $\tilde{\mathbf{X}}$ is done according to the following rule: if the fraction of the cell area occupied by metal on interface m is less than $\frac{1}{2}$, then we select $\mathbf{J}_m^{tan}$ as the variable of interest, otherwise we select $\mathbf{E}_{mB}^{tan}$. Then, after setting $\mathbf{J}_m^{tan} = 0$ and $\mathbf{E}_m^{tan} = 0$ over non metalized and metalized areas respectively, we can form a *reduced* system by retaining only the remaining non-zero elements of $\tilde{\mathbf{X}}$ and the zero elements of $\tilde{\mathbf{Y}}$. This leads to the desired square system:

$$\tilde{\mathbf{M}}_{Hred} \tilde{\mathbf{X}}_{red} = 0 \tag{24}$$

Re-arrangement of $\tilde{\mathbf{M}}_E$ into $\tilde{\mathbf{M}}_H$ requires multiplications and inversions of sub-matrices. These operations are performed in the transformed domain to take advantage of sparsity.

7) Source excitation leading to a particular solution: Any specific application in which the source can be formulated in terms of either a distribution of tangential electric field and/or surface current density on all or part of one of the interfaces can be represented using (21). Section IV explains how the sources

in the FSS and antenna array applications can be formulated as such.

The application of a distribution of tangential source electric fields in a slot cut in one of the metalized interfaces is equivalent to an applied magnetic current on both sides of the un-slotted metal interface. On the other hand, the application of a surface electric current distribution on a portion of one of the interfaces is equivalent to imposing a discontinuity in the tangential magnetic field on that portion of the interface.

Once the desired source has been written in terms of the $\tilde{\mathbf{X}}$ or $\tilde{\mathbf{Y}}$ generic vectors, it is inserted as a constant into equation (21), which is re-written by transferring all constants on the right-hand side. The application of the reduction process results in the following system of equations:

$$\tilde{\mathbf{M}}_{Hred'}\tilde{\mathbf{X}}_{red'} = \tilde{\mathbf{B}}_{red'} \tag{25}$$

which has as many unknowns as equations and has a unique solution.

III. Iterative Resolution Technique

In order to obtain a solution to (25), one would normally use the LU decomposition technique. However, the high number of unknowns generated with highly discretized interfaces results in memory and computing time difficulties. For example, a typical single-substrate patch antenna array problem analyzed with a discretization of 160×160 per periodic cell would typically result in a system of equations comprising $17,000$ unknowns when the reduction scheme is applied. The mere storage of a $17,000 \times 17,000$ complex matrix $\tilde{\mathbf{M}}_{Hred}$ in double precision would require about 4.3 gigabytes (GB) of RAM, which is highly impractical even considering today's advanced computer technology. Even if this considerable amount of RAM was available, an LU decomposition would require nearly an hour and a half of computing time on a 200 MHz Pentium I processor.

This example emphasizes the need to resort to an iterative resolution algorithm, which allows great reductions in memory and computing time requirements. Using such an algorithm, the above-mentioned problem was resolved with only 25 megabytes (MB) of RAM, within 12 minutes of computing time on a 200 MHz Pentium I processor.

Figure 4 illustrates the proposed iterative resolution algorithm. It is based on the use of the Bi-CGSTAB2 routine included with the PCG library [11]. While this method usually provides fast resolution of large systems of equations, the primary intent for using it is to circumvent the computer memory issue mentioned above. In order to do so, the system matrix $\tilde{\mathbf{M}}_{Hred'}$ should not be explicitly represented in the spatial domain, as this would require a very large amount of memory (4.3 GB of RAM in the above-mentioned example). Instead, the matrix operation $\tilde{\mathbf{M}}_{Hred'}\tilde{\mathbf{X}}_{red'}$ should be performed in the transformed domain, where all sub-matrices are diagonal.

It should be emphasized that, although this iterative resolution technique was primarily chosen in order to reduce the memory requirements, it has also proven to be a very fast way to resolve such systems.

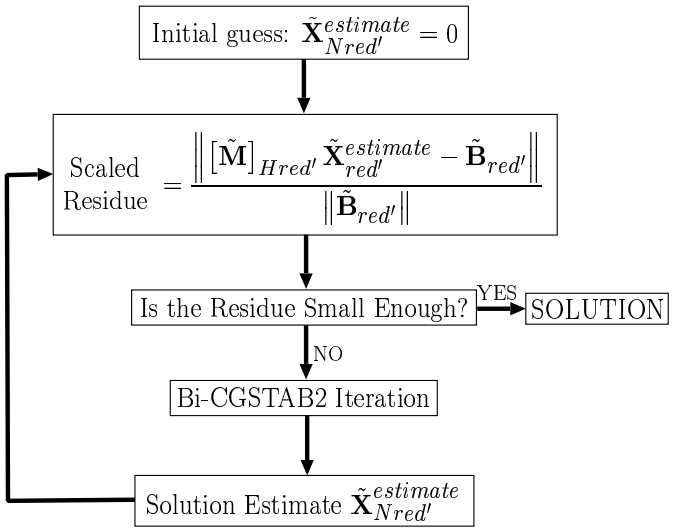

Fig. 4. Depiction of the iterative resolution algorithm.

IV. Analysis of Frequency Selective Surfaces

In the analysis of periodic multilayered FSS structures such as the one illustrated in Figure 1(a), we are interested in finding out the reflection and transmission coefficients for an incoming plane wave with an incidence angle α_i with respect to $\hat{y}$ and a plane of incidence making an angle ϕ_i with respect to $\hat{x}$. If we choose the periodicity such that there are no grating lobes, the only fields present in the far-field region are the incoming, reflected and transmitted plane waves. We will only present the developments and results for the TE polarization here; for the TM case, the reader should consult [12].

A. Definition of TE excitation

In order to analyze FSS structures, the general method that was defined in section II will be combined with a specific definition of the source for this particular problem, as explained in II-D.7. The Transverse electric (TE) excitation is illustrated in Figure 5. Our general formalism requires that the excitation be expressed in terms of total tangential fields. Since in the present case the physical source is an incident plane wave, we can only formulate a total fields source in the far-field region of the antenna, where the only contribution to the electromagnetic fields are the incident and reflected plane waves, provided that the element spacing is chosen such that no grating lobes are generated by the array. A thick free-space dielectric layer is added in the simulation model on top of the real structure and the total tangential electric fields are specified on top of it.

The electromagnetic fields of the incident plane wave for the TE case are:

$$\vec{e}^{\,i}_{TE}(x,y,z) = E_0 e^{-j(k_{x0}x + k_{yi}y + k_{z0}z)} \times \left(-\hat{x}\cos\alpha^i\cos\psi^i + \hat{y}\sin\alpha^i - \hat{z}\cos\alpha^i\sin\psi^i\right) \tag{26}$$

$$\vec{h}^{\,i}_{TE}(x,y,z) = \frac{\sqrt{\epsilon_{r0}}}{\eta_0} E_0 e^{-j(k_{x0}x + k_{yi}y + k_{z0}z)} \times \left(\hat{x}\sin\psi^i - \hat{z}\cos\psi^i\right) \tag{27}$$

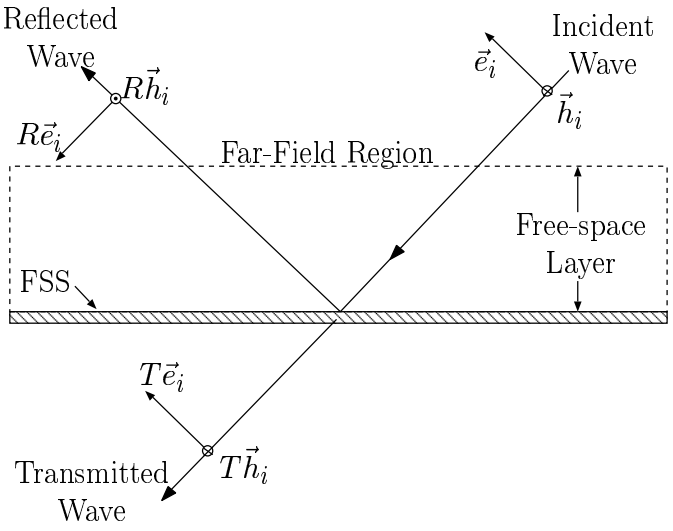

Fig. 5. Transverse electric (TE) plane wave incident upon a periodic frequency selective surface.

where E_0 refers to an arbitrary amplitude taken on top of the free-space layer, α^i and ψ^i refer to the incidence angles shown on Figure 1(a) and the propagation constants can be written in terms of those angles:

$$k_{x0} = -\sqrt{\epsilon_{r0}}k_0 \sin\alpha^i \cos\psi^i \tag{28}$$

$$k_{yi} = -\sqrt{\epsilon_{r0}}k_0 \cos\alpha^i \tag{29}$$

$$k_{z0} = -\sqrt{\epsilon_{r0}}k_0 \sin\alpha^i \sin\psi^i \tag{30}$$

with $k_0 = \frac{2\pi}{\lambda_0}$. The total tangential electric and magnetic fields on top of the free-space layer (i.e. at $y = y_{top}$) can thus be written as:

$$\vec{e}_{tan}(x,z) = \overbrace{(1+R)\,E_0 e^{-jk_{yi}y_{top}}}^{e^0_{tan}} e^{-j(k_{x0}x+k_{z0}z)} \times \left(-\hat{x}\cos\alpha^i\cos\psi^i - \hat{z}\cos\alpha^i\sin\psi^i\right) \tag{31}$$

$$\vec{h}_{tan}(x,z) = \overbrace{(1-R)\,\frac{\sqrt{\epsilon_{r0}}}{\eta_0}E_0 e^{-jk_{yi}y_{top}}}^{h^0_{tan}} e^{-j(k_{x0}x+k_{z0}z)} \times \left(\hat{x}\sin\psi^i - \hat{z}\cos\psi^i\right) \tag{32}$$

where R is the reflection coefficient of the FSS.

In order to obtain a numerical value for the reflection coefficient R, a total tangential electric field source (31) with arbitrary amplitude e^0_{tan} is used as the specified source in the simulation instead of an incident wavefield. The simulation results will then allow us to confirm that the tangential magnetic field on top of the free-space layer is of the form specified by (32). The resulting magnetic field amplitude h^0_{tan} can then be used to compute the reflection coefficient R using a well-known transmission line relationship:

$$R = \frac{Z_{tan} - \eta_0/\sqrt{\epsilon_{r0}}}{Z_{tan} + \eta_0/\sqrt{\epsilon_{r0}}}, \quad \text{with} \quad Z_{tan} = \frac{e^0_{tan}}{h^0_{tan}}. \tag{33}$$

The transmission coefficient T can be obtained simply by comparing the amplitude of the fundamental spectral component of the transmitted wave's tangential electric field to that of the incident wave, E_0. If all the dielectric and metallic layers are lossless, the results for R and T should obey the following conservation of power law:

$$|R|^2 + |T|^2 = 1 \tag{34}$$

R and T are determined independently from the simulation results, that is, (34) is not assumed *a priori*, it is a consequence of the fact that the proposed analysis technique conserves power, as it should. The verification of this relationship provides a validation checkpoint for the proposed analysis technique.

B. Numerical results for an array of metallic strips

Our modeling technique is first tested with a relatively simple structure (see Figure 6) of a linear periodic array of metallic strips printed on a dielectric substrate and forming a simple FSS. The physical parameters for this structure are the dielectric permittivity ϵ_r, the substrate thickness d, the strip width W_{strip} and the periodic cell width W_{cell}.

In order to provide a validation for our algorithm, we compare our results with those presented in [14], which were obtained using a "*Single-edge mode expansion*". Here, $d/\lambda_0 = 0.1$, $\epsilon_r = 2.0$ and the strips are positioned with a period of $0.3\lambda_0$. The simulated results are in terms of the power reflection ($|R|^2$) and transmission ($|T|^2$) coefficients as a function of the relative strip width, for the case of a plane wave incident with $\alpha_i = 30^\circ$ and $\psi_i = 0$. Since we need to sample the results over a range of strip widths, we may do so with a relatively good accuracy even for small discretization numbers, provided that the sample widths are chosen such that they allow a positioning of the lines compatible with the optimal edge parameter given in [6] ($p = 0.25$ [1]), which is valid for structures comprising metal discontinuities in a single direction.

Doing this, we obtain results that fit surprisingly well with the results of [14], even for very coarse discretization, as is shown on Figure 7. The only points that are somewhat off

[1] p is defined as the fraction of the discretization interval comprised between the edge of a metal strip in the model and the closest E-field line passing through the metal layer in the vicinity of the edge.

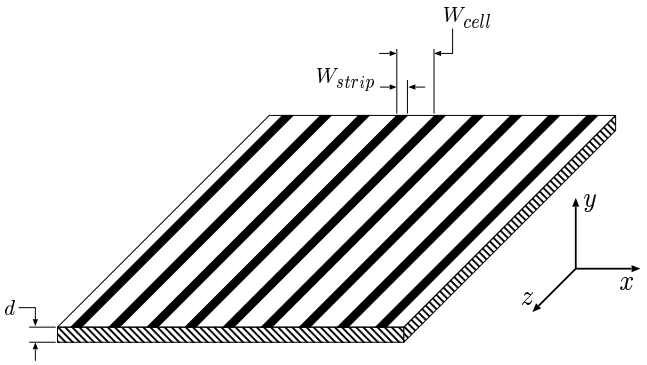

Fig. 6. A truncated section of a linear periodic array of metallic strips that form a simple frequency selective surface.

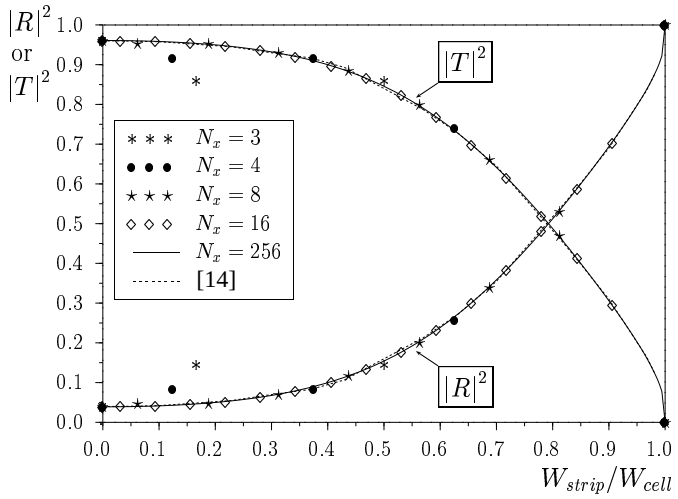

Fig. 7. Power reflection ($|R|^2$) and transmission ($|T|^2$) coefficients as a function of relative strip width for a plane wave incident with $\alpha_i = 30°$ and $\phi_i = 0$ on a linear array of infinitely long metallic strips. The strips are located at $0.3\ \lambda_0$ intervals and deposited on a dielectric substrate with a thickness $d = 0.1\lambda_0$ and a relative permittivity $\epsilon_r = 2$.

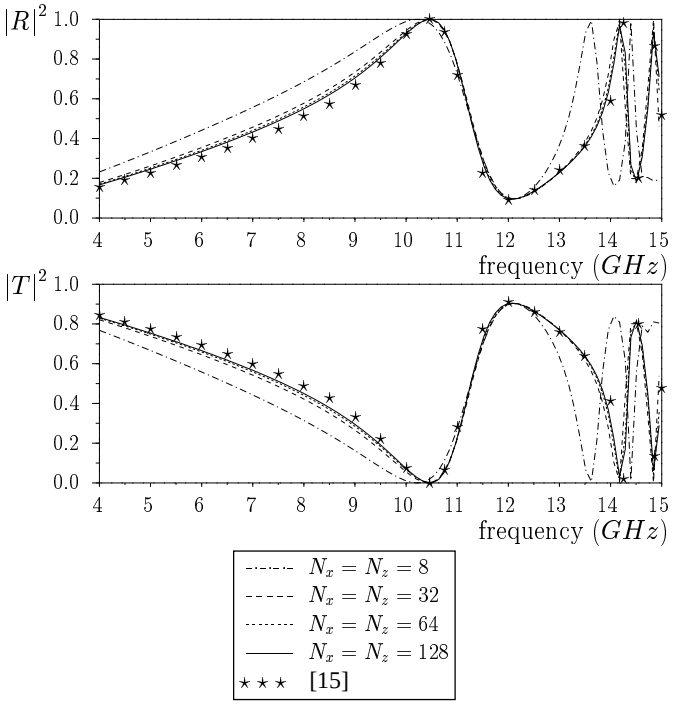

Fig. 8. Power reflection ($|R|^2$) and transmission ($|T|^2$) coefficients as a function of frequency for a plane wave with normal incidence on a planar array of metallic patches. The $1\ cm \times 1\ cm$ patches are located at $2\ cm$ intervals along both directions and deposited on a dielectric substrate with a thickness $d = 0.2\ cm$ and a permittivity $\epsilon_r = 3.5$.

the reference curve are for discretization levels of 3 and 4 lines per cell. In addition, we confirm that the power conservation law (34) holds for the two coefficients that were computed independently.

C. Numerical results for an array of metallic patches

The structure considered here is that of Figure 1(a), that is, a periodic planar array of rectangular metallic patches printed on a dielectric substrate. This is still a very simple structure, since it only features one dielectric substrate; we use it again as a validation case for our more general algorithm which supports multi-layer structures. The physical parameters for this structure are the dielectric permittivity ϵ_r , the substrate thickness d, the patch dimensions $P_x \times P_z$ as well as the patch spacings, or periodic cell dimensions, $L_x \times L_z$.

Here we will consider fixed physical dimensions and look at the power reflection and transmission coefficients as a function of frequency. The $1\ cm \times 1\ cm$ patches are positioned with a period of $2\ cm$ in each direction. It turns out that, for this particular ratio $P_x/L_x = P_z/L_z = \frac{1}{2}$, the use of *odd* numbers for the discretization levels N_x and N_z corresponds to an edge parameter value $p = 0.25$ [6], which would correspond to the optimal value if the edges were infinitely long. Since this is never the case, the edge parameter can not be tuned that well for arbitrary sized patches and cell sizes. Consequently, we intentionally choose to use *even* numbers for N_x and N_z in order to force the non-respect of the edge parameter prescriptions and find out what it implies in terms of convergence. In other tests not reported here, it was determined that convergence of the results as a function of the discretization level is slowed down when non-optimal values of the edge parameter are used.

Figure 8 shows the simulation results as a function of frequency, compared against results reported in [15] based on an analysis performed using the method of moments. The results compare well with the references; the slight remaining difference could be attributed to the limited discretization that was used in [15], where 15 rooftop basis functions per wavelength were used to discretize the metallic patch. This is much less than the level of discretization used here, which is in the range between 480 (at 4 GHz) and 1280 (at 15 GHz) samples per wavelength for the results shown in Figure 8. Such high discretization level required to obtain convergence would be a problem if a regular inversion technique was used, since it involved $8,320$ unknowns per frequency point. However, use of the iterative technique allowed to resolve this system of equations, comprising a $8,320 \times 8,320$ matrix, in an average time of 165 seconds per frequency point using a $200\ MHz$ Pentium I desktop computer and less than 15 MB of memory.

V. Analysis of Slot-Coupled Periodic Antenna Arrays

The same core analysis tool can be used as well for the analysis of periodic antenna arrays, provided that new source models are adapted to the general model (see section II-D.7). We will consider two types of sources. The first one, described in V-A, is an ideal and simple source that, although non-practical, provides a good validation of the core analysis tool, since macroscopic effects at the input port are mostly independent of the nature of the source. The second source, considered in V-B, is an actual physical feeding technique called "microstrip slot coupling" that requires a more involved model based on the reciprocity theorem.

A. Simple magnetic current source (Imposed E-field in slots)

This simple source model consists of exciting z-oriented thin slots under each patch by imposing a uniform, x-directed elec-

tric field in them (see Figure 9). This is equivalent to applying a z-oriented magnetic current source on the dielectric side of the ground plane. The total electric field source that is applied as a source to the homogeneous system of equations can formally be written as:

$$e_x = \begin{cases} V_{source}/F_x & \text{in the slot} \\ 0 & \text{out of the slot} \end{cases} \tag{35}$$

where $|V_{source}|$ can be thought of as an ideal voltage source applied across the slot of width F_x. We define the antenna (or input) impedance at each of the elements' input port (the slot) as:

$$Z_{ant} = \frac{|V_{source}|^2}{P^*_{ant}} \tag{36}$$

where $|V_{source}|$ is the amplitude of the source and P_{ant} is the complex power emitted by this source through one slot. This power is computed from the fields solution obtained using the core MoL-based analysis tool described in section II:

$$P_{ant} = \int_{S_{slot}} [e_z(x,z)h^*_x(x,z) - e_x(x,z)h^*_z(x,z)]\,dxdz \tag{37}$$

where S_{slot} is the area of the slot. The resulting impedance is an *active* impedance since it is obtained while all slots in the array are fed simultaneously with the proper phasing corresponding to the desired main beam pointing direction.

Consider a source that is matched at broadside in order to provide maximum power transfer; thus, the source impedance has to be $Z_s = Z^*_{ant}(\alpha = 0°)$. The reflection coefficient of the power wave [16] sent by the source thus becomes:

$$\Gamma_P(\alpha) = \frac{Z_{ant}(\alpha) - Z^*_s}{Z_{ant}(\alpha) + Z_s} = \frac{Z_{ant}(\alpha) - Z_{ant}(0°)}{Z_{ant}(\alpha) + Z^*_{ant}(0°)} \tag{38}$$

The value of $|\Gamma_P|^2$ corresponds to the fraction of power that is reflected by the antenna element to the source.

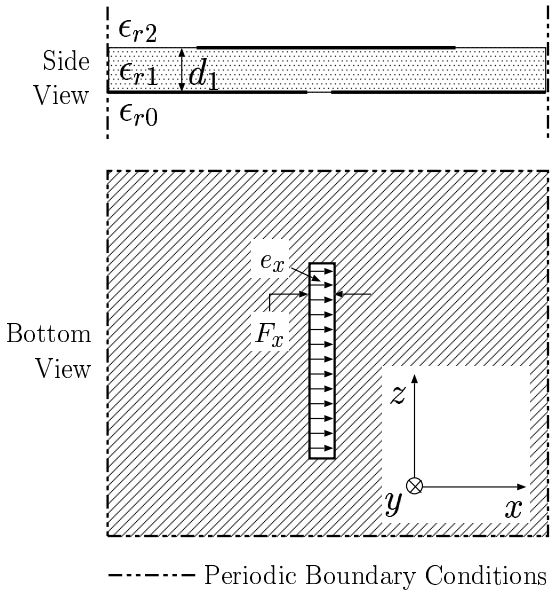

Fig. 9. Ideal tangential electric field source in a slot.

Figure 10 presents the graphs of the computed values for the amplitude of the power wave reflection coefficient $|\Gamma_P|$ for a planar array of rectangular patch antennas. Three planes were scanned, and graphical comparison with the results of [4] is included. The substrate used being relatively thick, it emphasizes the effect of the excitation of the TM_0 surface wave mode, that is excited at a scan angle of $\alpha = 68.9°$ in the E-plane. This *blindness* angle of the antenna can be predicted using dielectric waveguide theory [17], and is accurately predicted by our model, as seen on figure 10.

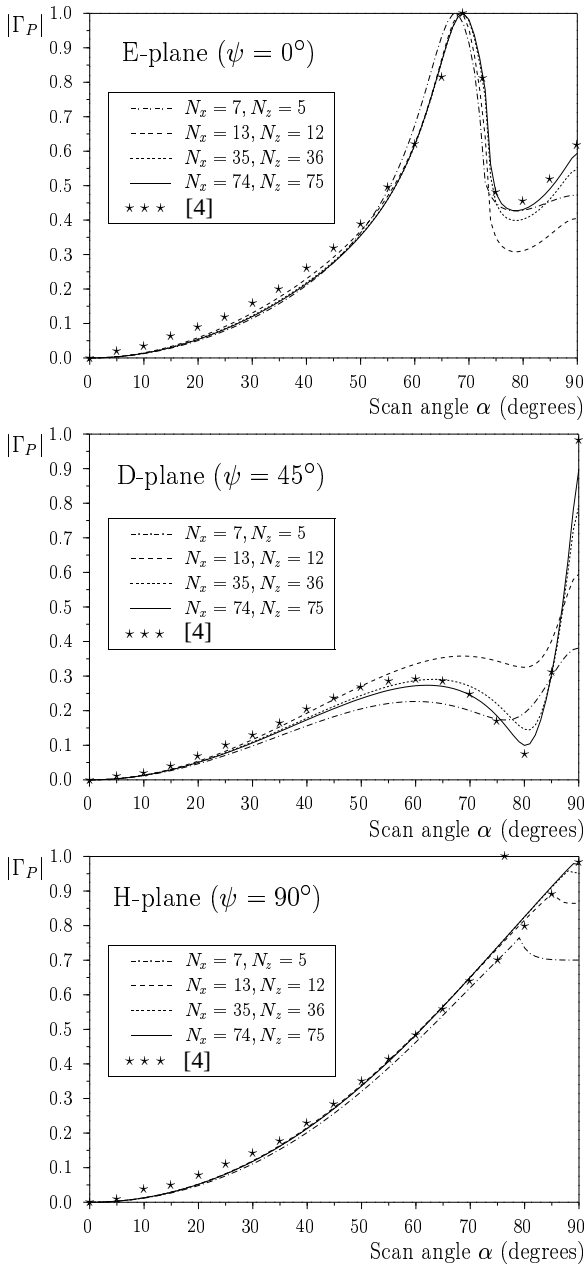

Fig. 10. Amplitude of power wave reflection coefficient $|\Gamma_P|$ as a function of the antenna main beam scan angle. The $0.28\ \lambda_0 \times 0.3\ \lambda_0$ patches are spaced $0.51\ \lambda_0$ in the x direction and $0.5\ \lambda_0$ in the z direction. They are deposited on a dielectric substrate with a thickness $d = 0.06\ \lambda_0$ and a permittivity $\epsilon_r = 2.55$. The patches are excited by $0.01\ \lambda_0 \times 0.115\ \lambda_0$ slots in the ground plane, in which a uniform E_x-field is imposed. The case with the largest discretization ($N_x = 74, N_z = 75$) involved $3,604$ unknowns per data point; each point was computed in 47 seconds on a Pentium I processor clocked at 200 MHz.

One single data point from [4] on the H-plane scan at $\alpha = 76.4^\circ$ disagrees significantly with our results. This discrepancy can be attributed to the different type of source that was used in [4]. A probe feeding technique was considered, which allows coupling of the TM_0 surface wave in all directions. Since our source only comprises an electric field in the x direction, it could not excite the TM_0 surface wave in the H-plane. Other than that particular data point, the results obtained with the highest discretization compare well with the reference values.

In addition to the prediction of the blindness angle in the E-plane and the validation with reference results, another expected feature for this specific structure was predicted by the model. As noted in Figure 10, the element spacing along the x-direction is $L_x = 0.51\lambda_0$, which means that grating lobes can be excited. The fact that we do not obtain a total power reflection at endfire ($\alpha = 90^\circ$) in the E-plane is consistent with the excitation of a grating lobe pointed near endfire.

B. Microstrip line slot coupling

The geometry of the microstrip line coupling of slots is illustrated in Figure 11. It consists of sending a signal on a microstrip line printed on the bottom substrate that couples to the patch antenna through a slot in the ground plane between the two substrates.

1) Formulation of the source using reciprocity: Because periodic boundary conditions do not allow for the representation of a microstrip line which continues outside the basic periodic cell, the microstrip feed line could not be directly included in the metalization patterns that is used within our core analysis technique described in section II. Instead, a technique using reciprocity, used in [18] with the method of moments, was adapted for use with the method of lines. This technique allows representation of the microstrip line coupled slot by a series impedance on the microstrip transmission line. The length of the stub following the slot is used to tune out the reactive part of the impedance, whereas the dimensions of the slot itself are used to match the series resistance to the characteristic impedance of the microstrip transmission line.

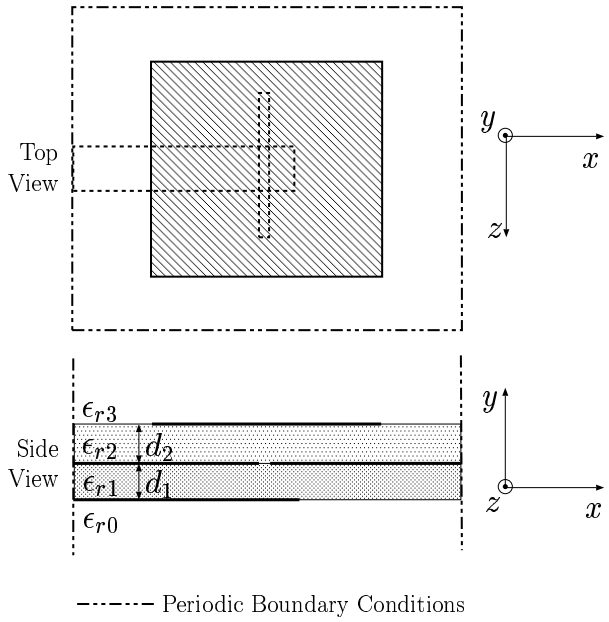

Fig. 11. Microstrip line coupling of a rectangular patch antenna through a slot in the ground plane.

In order to obtain a value for the equivalent series impedance, an analysis based on the reciprocity principle is performed where we consider an infinitely long microstrip transmission line coupled to a slot. From this procedure, the coefficient of reflection characterizing the discontinuity created by a z-directed thin slot centered on an x-directed microstrip line is obtained as ([12], [18], [19]):

$$R = -\frac{1}{2}\int_{slot\ area} e_x^s(x,z)h_z^{mic}(z)dxdz \tag{39}$$

where e_x^s represents the actual x-directed electric field in the slot, and h_z^{mic} represents the z-directed magnetic field in the ground plane of a microstrip line carrying an incident wave with a power of 1 Watt when no slots are present. The normalized magnetic field distribution $h_z^{mic}(z)$ can be determined from a 2D analysis of the microstrip transmission line; for the present work, this was done by implementing a standard formulation of the MoL with non-uniform discretization ([6],[12]).

The discretized version of (39), consistent with the notation used in II, can be written as the following:

$$R = -\frac{1}{2}\Delta_x\Delta_z\mathbf{E}^{\ell}_{x1B_{tot}}\cdot\mathbf{H}^{\ell\,mic}_{z1B_{slot}} \tag{40}$$

where $1B$ refers to the interface where the slot is present (see Figure 1). $\mathbf{H}^{\ell\,mic}_{z1B_{slot}}$ comes from discretizing $h_z^{mic}(z)$ and has no variations along the width of the slot. The total electric field component $\mathbf{E}^{\ell}_{x1B_{tot}}$ corresponds to that which is obtained from the excitation of the periodic structure (excluding the microstrip line) by a current density distribution $\mathbf{J}^{\ell}_{x1B} = -(1-R)\mathbf{H}^{\ell\,mic}_{z1B_{slot}}$ within the location of each slot. Since the value of R is not known prior to the simulation, the generic system can simply be excited with $\mathbf{J}^{\ell}_{x1B} = -\mathbf{H}^{\ell\,mic}_{z1B_{slot}}$, which should give a scaled response $\mathbf{E}^{\ell}_{x1B} = \dfrac{1}{1-R}\mathbf{E}^{\ell}_{x1Btot}$. In light of these observations, equation (40) can be re-written as a function of $\mathbf{E}^{\ell}_{x1B}$:

$$R = \frac{\Delta_x\Delta_z\mathbf{E}^{\ell}_{x1B}\cdot\mathbf{H}^{\ell\,mic}_{z1B_{slot}}}{\Delta_x\Delta_z\mathbf{E}^{\ell}_{x1B}\cdot\mathbf{H}^{\ell\,mic}_{z1B_{slot}} - 2} \tag{41}$$

Thus, it suffices to specify the source as a surface current distribution $\mathbf{J}^{\ell}_{x1B} = -\mathbf{H}^{\ell\,mic}_{z1B_{slot}}$ within the slot and to use the resulting response $\mathbf{E}^{\ell}_{x1B}$ together with (41) to compute the reflection coefficient on an infinite microstrip line caused by the presence of a slot in the ground plane.

2) Series impedance and stub tunning: Equation (41) assumes that the microstrip line has an infinite length. The equivalent series impedance along the line can be computed as:

$$Z_s = Z_{car}\frac{1+R}{1-R} - Z_{car} \tag{42}$$

where Z_{car} is the characteristic impedance of the microstrip line. If the line terminates at a distance L_{stub} from the slot,

we can consider it as a series open-circuit stub and compute the resulting input impedance:

$$Z_{in} = Z_s - jZ_{car}\cot\left(\beta_{mic}L_{stub}\right) \tag{43}$$

where β_{mic} is the propagation constant on the microstrip line. End effects on the line are neglected in this calculation. The wave reflection coefficient at the line input is thus obtained from:

$$S_{11} = \frac{Z_{in} - Z_{car}}{Z_{in} + Z_{car}} \tag{44}$$

where the phase reference is located in the center of the coupled slot.

3) Numerical results and validation: Here we present simulation results obtained using the microstrip coupling feed model. To provide validation of the model, results of a single-resonator periodic array antenna are compared with experimental measurements shown in [3] on a waveguide simulator where frequency sweeping allows for angular scanning of the main beam in the H plane ($\psi = 90°$) as prescribed by the relation $\alpha = \arcsin\left(\frac{\lambda_0}{4L_z}\right)$ which links the signal wavelength to the beam scan angle within the waveguide simulator, where L_z is the element spacing in the z direction.

a) Single resonator waveguide simulator*:* Figure 12 presents the results for the input impedance (input resistance R and reactance X) of such a structure. Numerical results are presented for four discretization levels, together with the experimental results from [3]. A single resonance appears on all curves, which is expected since we have a single resonator. The number of lines was carefully selected in such a way that the effective dimensions, computed using the line placement rules defined in [6], were as close as possible to the design dimensions of the patch and slot; this procedure, although not strictly necessary, speeds up convergence.

It is apparent that the converged simulated curve ($N_x = 220$, $N_z = 200$) approaches closely the shape and amplitude of the experimental curves, although there is a slight frequency shift of approximately 1.5 % between our simulation results and the experimental data reported in [3].

b) Dual resonator waveguide simulator*:* A dual-resonator patch antenna array featuring three dielectric slabs, of which one element is illustrated in Figure 13, was also simulated using the same model. The beam angle was linked to the signal wavelength, as prescribed earlier, in order to compare our results with published numerical simulation results [2]. Figure 14 presents the input impedance as a function of frequency. Again, the results present a good convergence behavior and agree fairly well with the reference data points from [2].

c) Single-frequency beam scanning of a single resonator patch array*:* Figure 15 shows the amplitude of S_{11} as a function of the antenna beam pointing angle for three scan planes. In order to compare our results with available data, we based our parameters on the geometry used in [3]. As pointed out in V-B.3.a, there is a slight discrepancy between the resonance frequency predicted by our code and that found in [3]. Since the patch has a fairly narrow resonance, a study of the beam scanning performed off resonance would not be a good indicator of the actual antenna performance. Impedance mismatch away from resonance may also hide the capability of our code

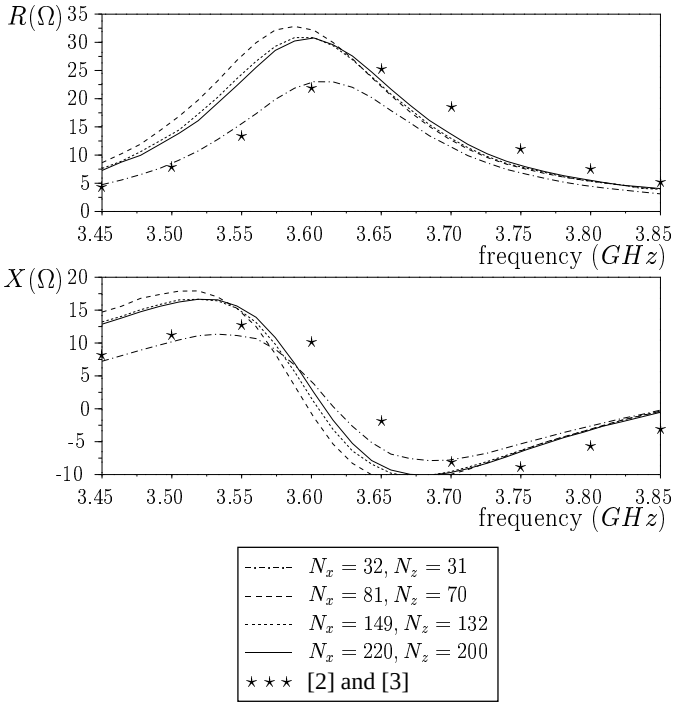

Fig. 12. Impedance (resistance R and reactance X) seen at the input of the microstrip line as a function of frequency for a single resonator patch antenna inside a waveguide simulator (similar to a periodic array of single resonators). The parameters used were: $\epsilon_{r0} = \epsilon_{r3} = 1$, $\epsilon_{r1} = \epsilon_{r2} = 2.2$, $d_1 = d_2 = 0.158$ cm, 2.5 cm × 2.5 cm patch resonator, 3.404 cm × 3.607 cm periodicity, 0.1 cm × 1.0 cm coupling slot, 0.49856 cm-wide microstrip (characteristic impedance of 50 Ω at 3.65 GHz) and 1.3 cm-long matching stub.

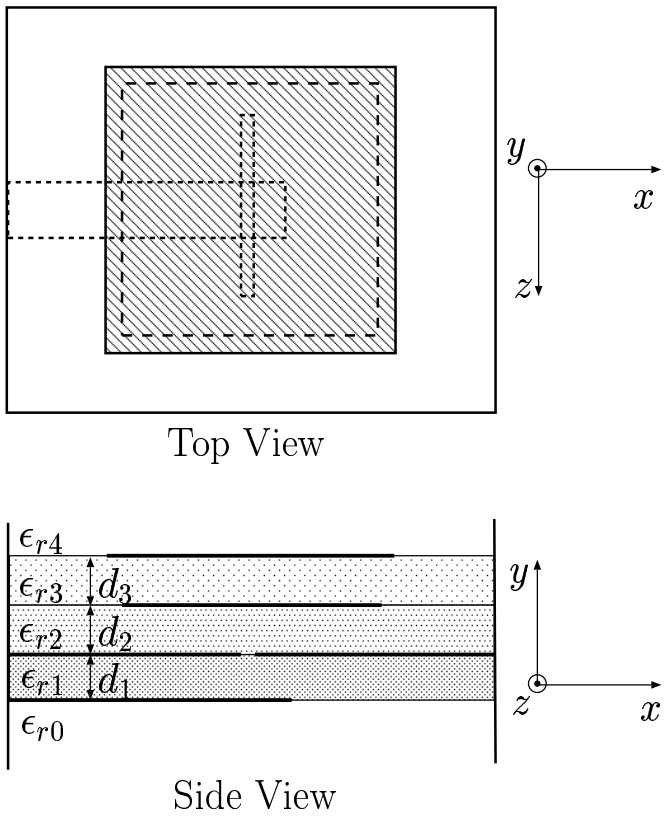

Fig. 13. Microstrip-coupled dual resonator patch antenna that constitutes one of the elements of a periodic array.

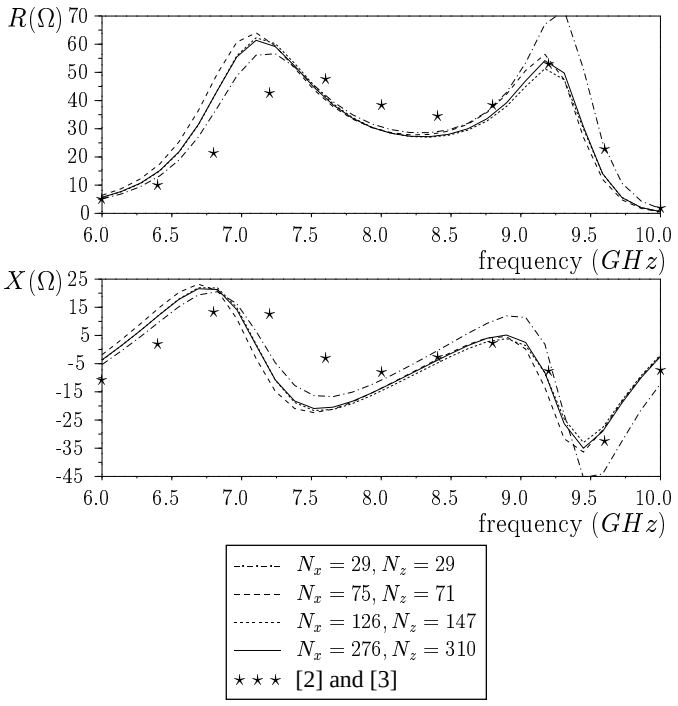

Fig. 14. Impedance (resistance R and reactance X) seen at the input of the microstrip line as a function of frequency for a dual resonator patch antenna inside a waveguide simulator (similar to a periodic array of dual resonators). The parameters used were: $\epsilon_{r0} = \epsilon_{r4} = 1$, $\epsilon_{r1} = \epsilon_{r2} = \epsilon_3 = 2.2$, $d_1 = d_2 = d_3 = 0.158$ cm, 0.9 cm × 0.9 cm inferior patch resonator, 1.0 cm × 1.0 cm superior patch resonator, 2.01 cm × 2.01 cm periodicity, 0.12 cm × 0.8 cm coupling slot, 0.51285 cm-wide microstrip (characteristic impedance of 50 Ω at 8.0 GHz) and 0.5 cm-long matching stub.

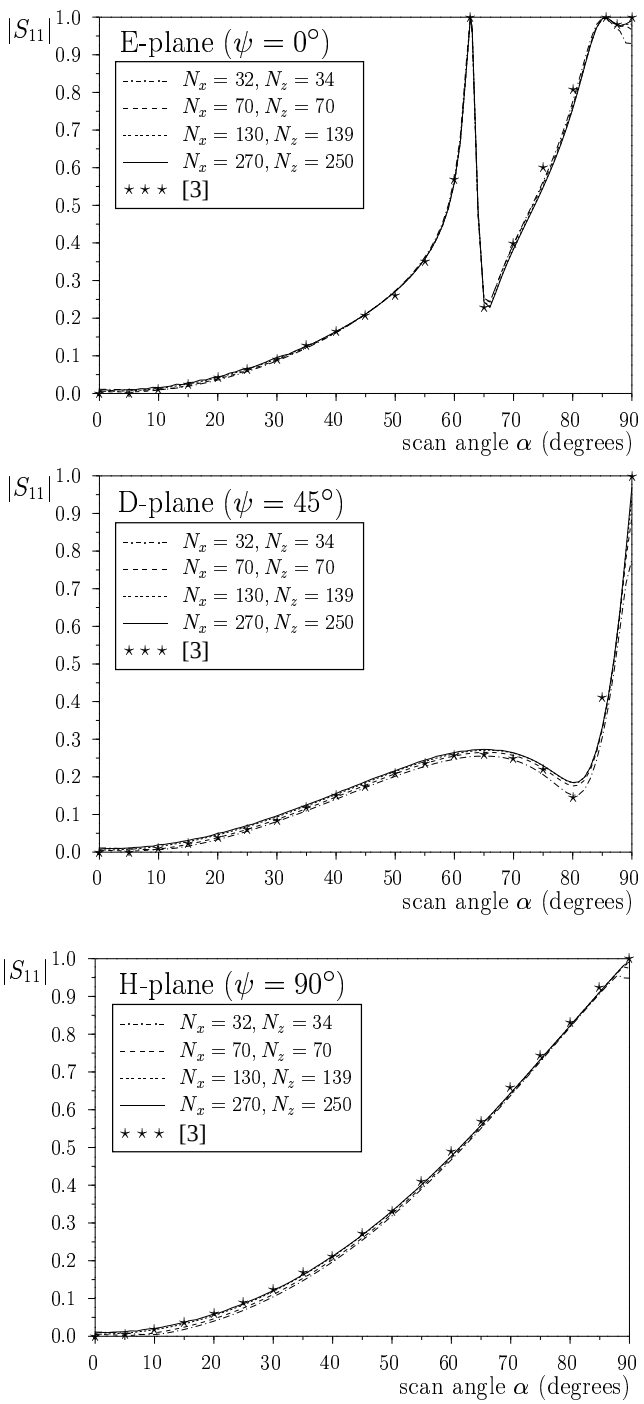

Fig. 15. Amplitude of the wave reflection coefficient S_{11} as a function of the beam incidence angle α in the three major planes E ($\psi = 0°$), D ($\psi = 45°$) and H ($\psi = 90°$). The parameters used were (ref. figure 11): $\epsilon_{r0} = \epsilon_{r3} = 1$, $\epsilon_{r1} = 12.8$, $\epsilon_{r2} = 2.55$, $d_1 = 0.05\lambda_0$, $d_2 = 0.02\lambda_0$, $0.275\lambda_0 \times 0.275\lambda_0$ patch resonator, $0.5\lambda_0 \times 0.5\lambda_0$ periodicity, $0.01\lambda_0 \times 0.113\lambda_0$ coupling slot, $0.04773\lambda_0$-wide microstrip line (characteristic impedance of 50 Ω) and $0.0701\lambda_0$-long matching stub for the highest discretization level.

to predict beam scanning effects. Consequently, it was decided, as one would do in a practical antenna design, to slightly adjust our patch dimensions to reach an impedance of 50 Ω at the normal scan angle ($\alpha = 0°$). Our patch dimensions are $0.275\lambda_0 \times 0.275\lambda_0$, compared to $0.29\lambda_0 \times 0.29\lambda_0$ in [3]. The chosen dimensions result in a maximization of the input resistance at every discretization level, which is then adjusted to 50 Ω by tuning the slot length to $0.113\lambda_0$ (compared to $0.115\lambda_0$ in [3]).

As stated earlier, the values for N_x and N_z (the total number of lines in both directions) were selected to get the most accurate effective dimensions. This process results in a trade-off between the discretization accuracy of the patch and slot, and there is no straightforward technique to predict the "overall accuracy" of the discretization for many discretized physical elements. Therefore, in the present case, N_x and N_z were selected such that the input resistance came close to 50 Ω at the broadside ($\alpha = 0°$) scan angle. In other words, the design parameters were effectively "tuned" for each discretization level by selecting the precise values for N_x and N_z. Nevertheless, for each of the discretization pairs (N_x,N_z) that were selected, the resulting discrete metallic patterns (patch and slot) constitute the best approximation, based on the line placement scheme prescribed in 1D problems, to a patch of dimensions $0.275\lambda_0 \times 0.275\lambda_0$ and a slot of dimensions $0.01\lambda_0 \times 0.113\lambda_0$. The length of a capacitive stub, implemented using the extent of the feed line overrunning the slot, was set independently for each discretization level to cancel the broadside input reactance. The required length tends to converge as the discretization is refined. For the N_x,N_z pairs shown on Figure 15, the required stub lengths were respectively $0.0667\lambda_0$, $0.0703\lambda_0$, $0.0708\lambda_0$ and $0.0701\lambda_0$. This is slightly smaller than the stub length of

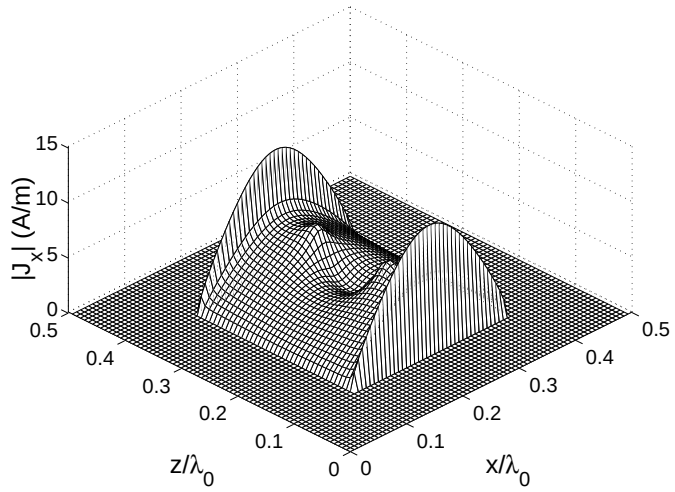

Fig. 16. Amplitude of the x-directed current density J_x in A/m at patch level for a slot-coupled patch resonator.

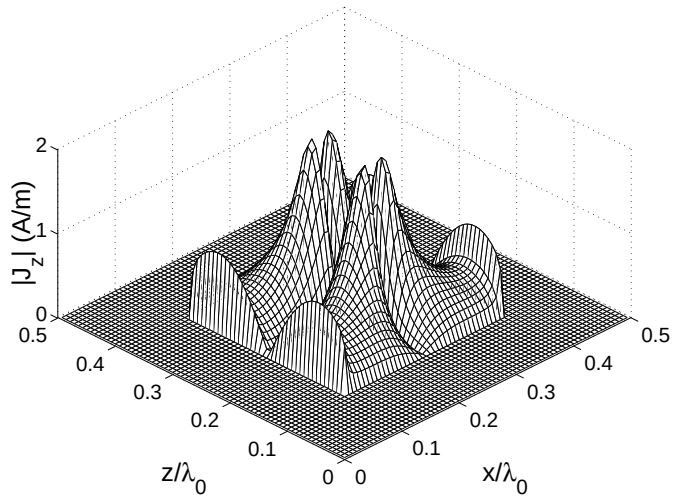

Fig. 17. Amplitude of the z-directed current density J_z in A/m at patch level.

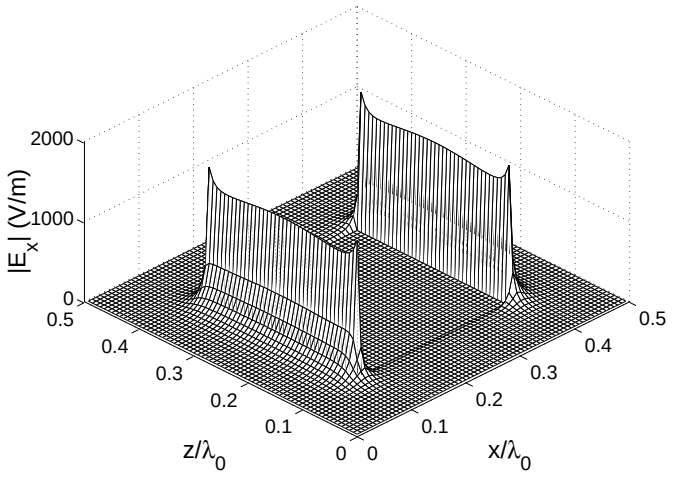

Fig. 18. Amplitude of the x-directed electric field E_x in V/m at patch level.

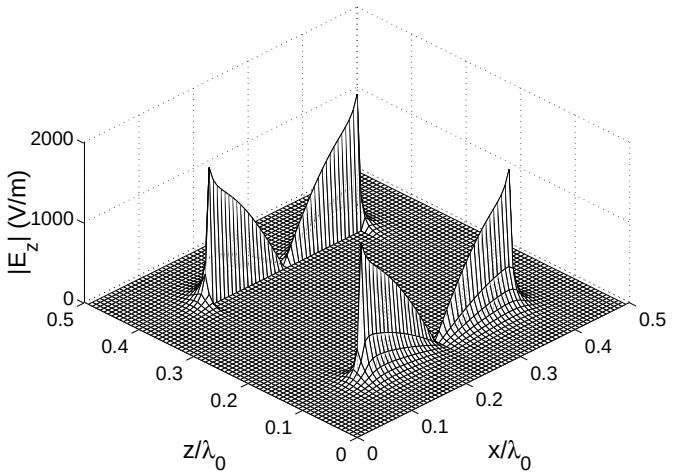

Fig. 19. Amplitude of the z-directed electric field E_z in V/m at patch level.

$0.075\lambda_0$ used in [3] and is attributed to the frequency shift discussed earlier.

This exercise demonstrates that the current model can be used as a design tool for a practical slot-coupled printed array antenna. As can be seen on Figure 15, the S_{11} parameter converges very quickly to the reference values, except near grazing incidence where a higher discretization is needed.

C. Sample E-field and current density distributions

All the parameters presented earlier (input impedance, reflection coefficient, etc.) were computed from the tangential electric field and current density distributions that constitute a solution to the problem. Looking at the sample distributions for J_x, J_z, E_x and E_z in figures 16 through 19 provides a good insight into the physics of the problem and, above all, serves as an additional figure-of-merit to confirm the validity of the proposed method, since the shapes of the illustrated distributions correspond to those usually encountered with patch antennas. The illustrated solution corresponds to the normal incidence case ($\alpha = 0°, \psi = 0°$) with the physical parameters given in section V-B.3.c. It was computed using a 70×70 grid.

VI. Conclusion

We presented a novel full-wave, modular approach based on the method of lines for the modeling of multilayered, periodic structures with realistic source models. The modularity of the approach allows for handling any given number of dielectric layers; here we showed applications with 1, 2 and 3 dielectric layers. It is also adaptable to multiple excitation schemes, provided that a proper source model is implemented and linked to the general model. We have done this for three different types of sources: an incoming wave for the FSS problem, an ideal slot excitation source, and a practical slot-coupling scheme. The adaptation of the reciprocity technique (presented in [18]) for use with the MoL, was key to the modeling of this widely used coupling technique. The functionality of our model was validated against published data pertaining to four particular structures: frequency selective surfaces composed of metallic strips and patches, and printed antenna arrays composed of microstrip-coupled single and dual resonator elements.

The uniform discretization scheme of the method of lines is attractive for its simplicity and because it can be applied to a very wide class of problems. However, its use often results in very large systems of equations because it is not tailored to any specific geometry. Such large systems can become intractable with conventional resolution techniques (e.g. Gauss elimination), both in terms of memory and computing time. One of the key aspects of this work is the combined use of an iterative technique and the FFT for the resolution of such large linear system. This approach greatly reduces the memory and computing time requirements, thereby rendering tractable, on a desktop computer, problems of this type involving tens of thousands of unknowns.

REFERENCES

[1] T. Pellerin, G. Séguin, and G. Brassard, "Active dual band dual polarized microstrip array panel," *Proceedings of the 1998 Symposium on Antenna Technology and Applied Electromagnetics*, August 1998, pp. 625–629.

[2] A. K. Bhattacharyya, "A numerical model for multilayered microstrip phased-array antennas," *IEEE Transactions on Antennas and Propagation*, vol. AP-44, no. 10, pp. 1386–1393, October 1996.

[3] D. M. Pozar, "Analysis of an infinite phased array of aperture coupled microstrip patches," *IEEE Transactions on Antennas and Propagation*, vol. AP-37, no. 4, pp. 418–425, April 1989.

[4] D. M. Pozar and D. H. Schaubert, "Analysis of an infinite array of rectangular microstrip patches with idealized probe feeds," *IEEE Transactions on Antennas and Propagation*, vol. AP-32, no. 10, pp. 1101–1107, October 1984.

[5] D. M. Pozar and D. H. Schaubert, "Scan blindness in infinite phased arrays of printed dipoles," *IEEE Transactions on Antennas and Propagation*, vol. AP-32, no. 6, pp. 602–610, June 1984.

[6] R. Pregla and W. Pascher, *Numerical techniques for microwave and millimeter-wave passive structures*, Chapter 6 - The Method of Lines, John Wiley-Interscience, 1989.

[7] H.Q. Zhu, Y. Long, and D.G. Fang, "Analysis of open planar structures using the method of lines with periodic boundary conditions," *Proceedings of IEEE Antennas and Propagation Society International Symposium*, 1995, pp. 786–789.

[8] Y. Long, H.Q. Zhu, and D.G Fang, "The fast algorithm of method of lines in analyzing the fss with oblique incidence," *Proceedings of IEEE Antennas and Propagation Society International Symposium*, 1995, pp. 2049–2052.

[9] R.S. Chen, E.K.N. Yung, C.H. Chan, and D.G. Fang, "Application of preconditioned cg-fft technique to method of lines for analysis of the infinite-plane metallic grating," *Microwave and Optical Technology Letters*, vol. 24, pp. 170–175, February 2000.

[10] E. Choinière and J.-J. Laurin, "Modélisation de réseaux d'antennes microruban par la méthode des lignes," 10^e *Journées Internationales de Nice sur les Antennes (JINA) - Conférences*, November 1998, pp. 350–353.

[11] W. D. Joubert, G. F. Carey, N. A. Berner, A. Kalhan, H. Kohli, A. Lorber, R. T. Mclay, and Y. Shen, *PCG Reference Manual - A Package for the Iterative Solution of Large Sparse Linear Systems on Parallel Computers*, Los Alamos National Laboratory, The University of Texas at Austin and University of Tennessee, 1.0 edition, September 1995.

[12] E. Choinière, "Modélisation de réseaux périodiques multicouches par la méthode des lignes," M. A. Sc. Thesis, École Polytechnique de Montréal, 1999, available from the National Library of Canada.

[13] A. Dreher and R. Pregla, "Full-wave analysis of radiating planar resonators with the method of lines," *IEEE Transactions on Microwave Theory and Techniques*, vol. 41, no. 8, pp. 1363–1368, August 1993.

[14] J. L. Volakis, Y. C. Lin, and H. Anastassiu, "TE characterization of resistive strip gratings on a dielectric slab using a single edge-mode expansion," *IEEE Transactions on Antennas and Propagation*, vol. AP-42, no. 2, pp. 205–212, February 1994.

[15] J.-M. Jin and J. L. Volakis, "Electromagnetic scattering by a perfectly conducting patch array on a dielectric slab," *IEEE Transactions on Antennas and Propagation*, vol. AP-38, no. 4, pp. 556–563, April 1990.

[16] G. Gonzalez, *Microwave Transistor Amplifiers*, Chapter 1, pp. 45–60, Prenctice Hall, 2^{nd} edition, 1997, Section 1.7: *Power waves and generalized scattering parameters*.

[17] C. A. Balanis, *Advanced Engineering Electromagnetics*, John Wiley & Sons, 1989.

[18] D. M. Pozar, "A reciprocity method of analysis for printed slot and slot-coupled microstrip antennas," *IEEE Transactions on Antennas and Propagation*, vol. AP-34, no. 12, pp. 1439–1446, December 1986.

[19] R.E. Collin and F. J. Zucker, *Antenna Theory, Part I*, Chapter 14, pp. 602–619, McGraw-Hill, 1969.

Éric Choinière (S'98) received the B. Eng. and M.A.Sc. degrees in electrical engineering from École Polytechnique de Montréal, Montreal, Quebec, Canada, in 1997 and 1999, respectively. He is currently working toward the Ph.D. degree in electrical engineering at the University of Michigan and is affiliated with the Radiation Laboratory and the Space Electrodynamics and Tether Systems Group. The research work that led to his M.S. thesis involved the development of a computational model for multilayered printed array antennas and frequency selective surfaces. His current research involves both the experimental testing and computational modeling of the electron collection processes to bare electrodynamic space tethers. He is a member of IEEE, the Applied Computational Electromagnetics society, the Microwave Theory and Techniques society and the Nuclear and Plasma Science society.

Jean-Jacques Laurin (S'87-M'91-SM'98) received the B.Eng. degree in engineering physics from École Polytechnique, Montreal, Quebec, Canada, in 1983, and the M.A.Sc. and Ph.D. degrees in electrical engineering from University of Toronto, Toronto, Ontario, Canada, in 1986 and 1991 respectively. In 1991, he joined the Department of Electrical and Computer Engineering, École Polytechnique de Montréal, where he is now Professor. During academic year 1998-1999, he was an Invited Professor at École Polytechnique Fédérale de Lausanne, Switzerland. His research interests are in the areas of antennas, microwave imaging and electromagnetic compatibility. He was member of the organizing committees of ANTEM'96, 1997 IEEE APS-URSI Symposium and ISMOT'2001. He was the Technical Papers Chairman of 2001 IEEE EMC Symposium. Dr. Laurin is a member of the Canadian National Committee of of URSI, representing Commission B. He is also a member of the Ordre des Ingénieurs du Québec.